Incorporating Darcy's law for pure solvent flow through porous tubes: asymptotic solution and numerical simulations

Nils Tilton, Denis Martinand, Eric Serre

Laboratoire M2P2, UMR 6181, Université Aix-Marseille, CNRS, 13451 Marseille, France

Richard Lueptow

Department of Mechanical Engineering,

Northwestern University, Evanston, IL 60208, USA

March 28, 2012

Abstract

A generalized solution for pressure-driven, incompressible, Newtonian flow in a porous tubular membrane is challenging due to the coupling between the transmembrane pressure and velocity. To date, all analytical solutions require simplifications such as neglecting the coupling between the transmembrane pressure and velocity, assuming the form of the velocity fields, or expanding in powers of parameters involving the tube length. Moreover, previous solutions have not been validated with comparison to direct numerical simulation. We comprehensively revisit the problem to present a robust analytical solution incorporating Darcy's law on the membrane. We make no assumptions about the tube length or form of the

velocity fields. The analytic solution is validated with detailed comparison to direct numerical simulations, including cases of axial flow exhaustion and cross flow reversal. We explore the validity of typical assumptions used in modelling porous tube flow and present a solution for porous channels in the supplementary material.

Topical Heading: Fluid Mechanics and Transport Phenomena
Keywords: Cross flow filtration, Darcy's law, Porous tube, Asymptotic expansion, Direct numerical simulation

Introduction

Pressure-driven fluid flow through a porous tube occurs in such diverse applications as filtration, aeration, sparging, foaming, membrane reactors, irrigation, transpiration cooling, and medical devices. The current study is motivated by filtration systems in which a suspension or solution is pumped axially through a tubular membrane, purified filtrate is extracted through the membrane, and concentrate exits downstream. The transmembrane flow is driven by the transmembrane pressure difference between the inner and outer surfaces of the porous tube. Filtration systems are often classified according to their membrane pore size and operating pressure[1]. Microfiltration systems, for example, have the largest pore sizes, 0.1 to 10 μm, and the lowest transmembrane pressures, up to 2 bars. Ultrafiltration systems have pore sizes ranging from 2 to 100 nm and transmembrane pressures up to 5 bars, nanofiltration systems have pore sizes ranging from 0.5 to 2 nm and transmembrane pressures up to 20 bars, while reverse osmosis systems have pore sizes less than 0.5 nm and transmembrane pressures up to 120 bars.

The current study improves the accuracy of the analytical solution for steady laminar flow of incompressible Newtonian fluids in porous tubes, and assesses the solution's validity domain by comparison to direct numerical simulations. We do

not consider the more complicated problem of solute or particle transport and related effects of concentration polarization and membrane fouling. Because of its fundamental nature and varied applications, fluid flow in a porous tube has been studied extensively. The problem remains challenging, however, due to the coupling between the transmembrane pressure and velocity with the simultaneous coupling between the axial pressure gradient and axial velocity. These couplings cause the axial pressure gradient, axial velocity, and transmembrane velocity to vary axially. An extreme example is a situation known as cross flow reversal (CFR), where the transmembrane flow reverses from suction to injection due to the axial pressure drop. A second example is axial flow exhaustion (AFE), in which the axial flow is exhausted due to transmembrane suction. CFR has applications in membrane bioreactors[2], while AFE occurs in dead-end filtration.

In most filtration systems, the radial velocity is small compared to the axial velocity, and variations of the flow field in the axial direction are small compared to those in the radial direction. Consequently, many analytical[3,4,5,6] and numerical[7,8,9] studies of porous tube and channel flows prescribe a uniform suction velocity that is independent of the pressure. This approach was originally suggested by Berman[10] for channel flows and has also been used in annular geometries.[11,12] It is physically incorrect, however, because the transmembrane pressure and velocity necessarily vary along the length of the tube. Other analytical solutions allow the transmembrane velocity to vary axially according to an assumed function that is independent of the pressure.[13,14] The results, however, require the axial variation of the transmembrane flow be determined experimentally.

More sophisticated analytical studies model the coupling between the transmembrane pressure and velocity using Darcy's law. These studies assume one or more physical quantities are small, so as to discard terms in the governing equations. Though not always stated explicitly, these studies use what may be interpreted as asymptotic expansions in which at least the leading-order expressions

for the pressure and velocity fields are computed. The leading-order solution, first demonstrated by Regirer[15], is now well established. The higher-order corrections, however, remain an open question. This is largely due to the diverse array of simplifying assumptions that have been used.

Regirer[15] assumes the radial Reynolds number and ratio between the radial and axial velocities is small. At higher orders, he also assumes the transmembrane velocity is a given function. Galowin and DeSantis[16] assume the radius to length ratio is small and the axial Reynolds number large. Kelsey *et al.*[2] also assume a small radius to length ratio as well as a small radial Reynolds number, and do not include the nonlinear convective terms in the Navier-Stokes equations. The "text-book" solution of Middleman[17] also neglects the convective terms and restricts the solution to small transmembrane velocities. Denisov[18] assumes the radial to axial velocity ratio times the length to radius ratio is small, as well as the ratio between the axial pressure drop and transmembrane pressure. He also approximates the transmembrane velocity as a polynomial function. Karode[19] assumes the predominant pressure gradient is in the axial direction, and the ratio of the axial to transmembrane flow rates is small. Borsi *et al.*[20] assume a small radius to length ratio, an axial Reynolds number of order unity or less, and a ratio between the transmembrane pressure and axial pressure drop of order unity or less. Kim and Lee[21] assume the radial Reynolds number is small. Galowin and DeSantis[16], Middleman[17], Karode[19], and Kim and Lee[21] assume the axial flux and pressure satisfy a local Hagen–Poiseuille law with a parabolic axial velocity profile. Granger *et al.*[22] solve the Navier-Stokes equation with an *ad hoc* iterative procedure that assumes axial and radial variations of the velocity and pressure fields are of the same order. This leads to inconsistencies in their higher-order corrections. Despite these various, sometimes conflicting, approaches, these studies yield similar, sometimes identical, expressions for the leading-order velocity and pressure fields.

Though some of the above studies consider higher-order terms in order to assess

the validity of the leading-order solution, none address the validity domain of their solutions with detailed comparison to experiment or direct numerical simulations. An exception is a study of flow in porous planar channels in which Haldenwang[23] incorporates Darcy's law by expanding the governing equations about the transverse Reynolds number and seeking a solution locally equal to that of Berman[10]. The analytical solution was found to agree well with numerical simulation.

We present a robust analytical formulation for steady, laminar, incompressible fluid flow through cylindrical porous tubes with Darcy's law on the permeable surface. The approach is similar to that used by Tilton *et al.*[24] for rotating filtration in Taylor-Couette cells. We assume that axial variations of the velocity field are small compared to variations in the radial direction, and we carefully address the relative order of terms in the equations of motion using an order-of-magnitude analysis. We seek a solution in the form of an asymptotic expansion about a small parameter related to the membrane permeability. We make the expansion robust using the following principles. The small parameter should be a physical quantity that reflects the validity of the expansion. The assumptions with regard to the small parameter should be as few as possible. The small parameter can be based on geometrical features and physical properties of the fluid and membrane. The small parameter should not be based on the field variables such as the velocity and pressure so that in critical cases such as CFR and AFE, these fields can vanish locally without the validity of the expansion being called into question. Assumptions regarding the system length should be avoided because increasing the system length, while keeping all other quantities constant, should not increase the accuracy of the expansion. Moreover, the validity domain of the approximation must be addressed by comparison with experimental or numerical results.

Our analytical solution makes no assumption about the system length, the form of the axial velocity profile, or transmembrane velocity. We confirm its validity by detailed comparison with direct numerical simulations using typical operating

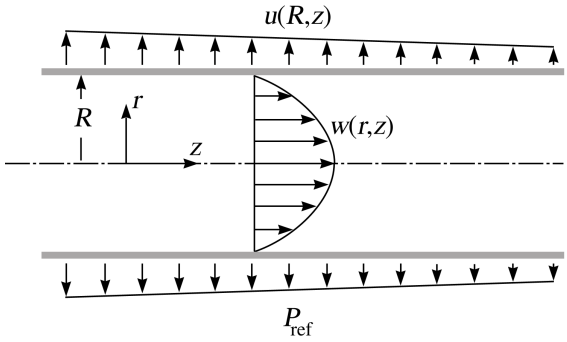

Figure 1: Sketch, not to scale, of the cylindrical geometry and laminar velocity profiles.

conditions for microfiltration and ultrafiltration as well as extreme cases of CFR and AFE. We demonstrate that our analytic solution includes the proper higher-order corrections for the velocity and pressure. This allows us to 1) explain the influence of the higher-order terms on the flow, 2) provide guidelines about when simplifying assumptions about the permeate flow may be used, and 3) give an easily-calculated exact solution for the spatially varying flow and pressure fields. Our analytic solution should provide a stronger basis for future examination of the influence of solutes or particles in situations where concentration polarization or other filtration phenomena occur, though we do not consider this here.

Geometry and governing equations

We consider steady, axisymmetric, incompressible fluid flow within a stationary circular tube of internal radius R, as illustrated in figure 1. The tube is made of a permeable membrane of thickness h. We assume the fluid region outside the tube, $r > R+h$, is maintained at a constant uniform pressure P_{ref}, as is the case for most cross-flow filtration systems where the filtrate exits the membrane to atmospheric pressure, with no effects due to surface tension. Without loss of generality, we set $P_{\text{ref}} = 0$. An axial pressure gradient drives an axial Poiseuille flow $w(r, z)$, while the transmembrane pressure difference drives radial suction or injection $u(R, z)$. As in all previous analytical studies of flow through tubular membranes, we do not

address inlet and outlet regions where the flow may be undeveloped.

The governing equations are the steady, axisymmetric, Navier-Stokes and continuity equations,

$$u\frac{\partial u}{\partial r} + w\frac{\partial u}{\partial z} + \frac{1}{\rho}\frac{\partial p}{\partial r} - \frac{\mu}{\rho}\left(\frac{\partial^2 u}{\partial r^2} + \frac{1}{r}\frac{\partial u}{\partial r} - \frac{u}{r^2} + \frac{\partial^2 u}{\partial z^2}\right) = 0, \tag{1}$$

$$u\frac{\partial w}{\partial r} + w\frac{\partial w}{\partial z} + \frac{1}{\rho}\frac{\partial p}{\partial z} - \frac{\mu}{\rho}\left(\frac{\partial^2 w}{\partial r^2} + \frac{1}{r}\frac{\partial w}{\partial r} + \frac{\partial^2 w}{\partial z^2}\right) = 0, \tag{2}$$

$$\frac{\partial u}{\partial r} + \frac{u}{r} + \frac{\partial w}{\partial z} = 0, \tag{3}$$

where p, ρ, and μ are the fluid pressure, density, and dynamic viscosity, respectively. On the surface $r = R$, we apply the no-slip condition and Darcy's law,

$$w = 0, \quad u = \frac{k}{\mu h}p, \quad \text{on} \quad r = R, \tag{4}$$

where k is the membrane permeability of units length squared.

To close the system of equations, it is sufficient to prescribe either the mean axial velocity or the transmembrane pressure at two arbitrary axial locations, or to prescribe both the mean axial velocity and the transmembrane pressure at a single axial location. Guided by typical inlet or outlet conditions for a laboratory experiment, we illustrate the solution procedure by prescribing the transmembrane pressure, P_{tm}, and mean axial velocity, $\overline{W}_0$, at the arbitrary axial location $z = 0$,

$$P_{\text{tm}} = p\Big|_{r=R}, \quad \overline{W}_0 = \frac{1}{\pi R^2}\int_0^R w 2\pi r \mathrm{d}r, \quad \text{on} \quad z = 0. \tag{5}$$

The solution is equally valid for positive and negative values of z. Thus, $z = 0$ can correspond to any axial location, including the midpoint along the length of the tube, which we use for convenience in the comparison of our analytic solution with numerical simulations. The solution procedure can be easily revised for other inlet or outlet conditions. In section , we include the solution for a dead-end filtration

of system length L_s and mean axial inlet velocity of $\overline{W}_0$. This requires,

$$\overline{w}\Big|_{z=0} = \overline{W}_0, \qquad \overline{w}\Big|_{z=L_s} = 0. \tag{6}$$

Flows over permeable surfaces may have a non-zero tangential velocity at the surface due to momentum transfer to the fluid within the porous material. This tangential velocity is important when a streamwise pressure gradient drives a streamwise flow within the porous material.[25] In a study of unsteady flow in tubular membranes, Borsi *et al.*[20] incorporated a tangential velocity on the membrane surface using the slip conditions of Beavers and Joseph.[25] These conditions, however, were derived for steady, fully developed, channel flows with negligible inertial effects and are limited to porous walls sufficiently thick to satisfy length scale constraints associated with volume-averaged quantities in the porous region.[25,26]

The no-slip assumption in equation (4) is valid when a membrane is made of small discrete holes such that the permeability is zero in the tangential directions and the percentage area of the pores on the surface is small. In membrane filtration flows, however, the no-slip assumption is often reasonable even when the membrane is made of an isotropic porous material, as is the case for many ceramic membranes, because the membrane permeability and porosity are typically very small. As a result, the transmembrane pressure necessary to drive even a small transmembrane velocity is several orders of magnitude higher than any streamwise pressure gradient. Consequently, though these membranes are isotropic, the flow within them is well approximated as purely radial. For these reasons, we do not consider slip because it plays only a negligible role in most filtration applications. For clarity, we stress that our results are applicable to membranes of any thickness, h, provided the transmembrane flow is well described by Darcy's law, and the no-slip assumption is a reasonable approximation at the membrane surface.

Asymptotic expansion

We seek a solution to equations (1)–(5) in the form of a regular asymptotic expansion when variations of the velocity field in the axial direction are small compared to those in the radial direction. The first, and arguably most important, step is an order-of-magnitude analysis to determine the relative importance of the various terms and suggest an optimal nondimensionalization[27]. For this purpose, we introduce the following characteristic scales,

$$u \sim U, \qquad w \sim \overline{W}_0, \qquad p \sim P, \qquad r \sim R, \qquad z \sim L, \tag{7}$$

where U, P, and L are characteristic scales that remain to be defined. We assume variations in the radial direction scale with R, while variations in the axial direction scale with L. We stress that L is not necessarily equal to the system length, as described shortly. Consistent with our assumption that axial variations of the velocity field are small compared to those in the radial direction, the ratio R/L is of order ϵ, where $\epsilon \ll 1$ is a small parameter that will be defined shortly. Note that following the discussion in the previous section, the membrane thickness, h, does not play a role in the order-of-magnitude analysis.

Applying (7) to the continuity equation (3), we find that

$$\frac{U}{\overline{W}_0} \sim \frac{R}{L} = \mathcal{O}(\epsilon). \tag{8}$$

Axial variations of the axial velocity field, $\partial w/\partial z$, are small when the characteristic transmembrane velocity is small compared to the characteristic axial velocity. Haldenwang[23] interprets relation (8) in terms of the dead-end length, L_{de}, from $z = 0$ where the axial flow is completely exhausted due to transmembrane suction. In systems for which the transmembrane velocity may be approximated as a

constant, $u(R,z) = u_{\rm tm}$, the dead end length may be approximated as

$$\frac{R}{L_{\rm de}} = 2\frac{u_{\rm tm}}{\overline{W}_0}. \tag{9}$$

The ratio $u_{\rm tm}/\overline{W}_0$ is of order 10^{-4} to 10^{-5} in ultrafiltration, nanofiltration and reverse osmosis studies,[1] and of order 10^{-2} to 10^{-4} in microfiltration studies.[28]

Applying (7) and (8) to the axial momentum equation (2), we find that

$$u\frac{\partial w}{\partial r} + w\frac{\partial w}{\partial z} \sim \epsilon\frac{\overline{W}_0^2}{R}, \qquad \frac{\mu}{\rho}\frac{\partial^2 w}{\partial z^2} \sim \epsilon^2\frac{\mu\overline{W}_0}{\rho R^2}, \tag{10}$$

$$\frac{1}{\rho}\frac{\partial p}{\partial z} \sim \frac{1}{\rho}\frac{P}{L}, \qquad \frac{\mu}{\rho}\left(\frac{\partial^2 w}{\partial r^2} + \frac{1}{r}\frac{\partial w}{\partial r}\right) \sim \frac{\mu\overline{W}_0}{\rho R^2}. \tag{11}$$

Because the axial pressure gradient drives the axial flow, and because from (8) we expect to recover Poiseuille flow in the limit $\epsilon \to 0$, the pressure term and viscous term in (11) must be of the same order. This requires that

$$P \sim \frac{\mu\overline{W}_0}{\epsilon R}. \tag{12}$$

The presence of ϵ in the denominator of (12) may appear counterintuitive. It is physically consistent, however, when P is interpreted as the characteristic transmembrane pressure. First, for the transmembrane velocity, $u_{\rm tm}$, to vary slowly in the axial direction, the change in pressure over a small axial length of the tube must be small compared to the transmembrane pressure. Second, as the permeability tends to zero, an infinite transmembrane pressure is required to drive a finite transmembrane velocity. Third, to recover Poiseuille flow as the permeability tends to zero, the axial pressure gradient, $\partial p/\partial z \sim P/L$, must be of order unity. These criteria are satisfied when P is inversely proportional to ϵ. A literature review finds that $\mu\overline{W}_0/(P_{\rm tm}R)$ is on the order of 10^{-5} to 10^{-6} for microfiltration,[28] and on the order of 10^{-7} to 10^{-8} for ultrafiltration, nanofiltration and reverse osmosis[1].

To investigate the axial variation of the transmembrane flow and pressure, we

take the derivative of Darcy's law with respect to z,

$$\frac{\partial u}{\partial z} = \frac{k}{\mu h}\frac{\partial p}{\partial z}, \quad \text{on} \quad r = R. \tag{13}$$

Applying relations (7), (8) and (12) to equation (13), we find that

$$\sigma \sim \frac{RU}{L\overline{W}_0}, \tag{14}$$

where $\sigma = k/(hR)$ is the nondimensional permeability. Equations (14) and (8) require that σ is of order ϵ^2. Thus motivated, we define

$$\epsilon = \sqrt{\sigma}, \qquad L = \frac{R}{\epsilon}. \tag{15}$$

In summary, conditions (8) and (12) reflect two physically different conditions necessary for the velocity fields to vary slowly in the axial direction. First, the transmembrane velocity must be small compared to the mean axial velocity, leading to the inequality $U/\overline{W}_0 \ll 1$. Second, the axial pressure gradient must be small compared to the transmembrane pressure, leading to the inequality $\sigma \ll U/\overline{W}_0$. Our definition (15) for ϵ and L ensures these conditions are satisfied. A literature review finds that σ varies between 10^{-10} and 10^{-14} for ultrafiltration, nanofiltration and reverse osmosis[1], and between 10^{-6} and 10^{-9} for microfiltration[28]. Therefore, $\epsilon = \sqrt{\sigma}$ is a physically natural parameter that satisfies our robustness criteria. It is a physical, geometrical, quantity that reflects the validity of the expansion and it is not based on the system length or the field variables.

Motivated by our order-of-magnitude analysis, we introduce the following nondimensionalized variables

$$\hat{u} = \frac{u}{\epsilon\overline{W}_0}, \qquad \hat{w} = \frac{w}{\overline{W}_0}, \qquad \hat{p} = \frac{\epsilon R}{\mu\overline{W}_0}p, \qquad \hat{r} = \frac{r}{R}, \qquad \hat{z} = \frac{z}{L}. \tag{16}$$

The nondimensionalization (16) is chosen so $\hat{u}$, $\hat{w}$, $\hat{p}$, $\hat{r}$, and $\hat{z}$ are expected to

be of order one. Later, we express the final analytical solution using a more traditional nondimensionalization. To avoid confusion, we continue using the $\hat{}$ symbol to denote all variables and parameters nondimensionalized using (16). The nondimensionalized governing equations and boundary conditions are,

$$\epsilon^3 \hat{u}\frac{\partial \hat{u}}{\partial \hat{r}} + \epsilon^3 \hat{w}\frac{\partial \hat{u}}{\partial \hat{z}} + \frac{2}{\mathrm{Re}}\frac{\partial \hat{p}}{\partial \hat{r}} - \frac{2\epsilon^2}{\mathrm{Re}}\left(\frac{\partial^2 \hat{u}}{\partial \hat{r}^2} + \frac{1}{\hat{r}}\frac{\partial \hat{u}}{\partial \hat{r}} - \frac{\hat{u}}{\hat{r}^2} + \epsilon^2\frac{\partial^2 \hat{u}}{\partial \hat{z}^2}\right) = 0, \tag{17}$$

$$\epsilon \hat{u}\frac{\partial \hat{w}}{\partial \hat{r}} + \epsilon \hat{w}\frac{\partial \hat{w}}{\partial \hat{z}} + \frac{2}{\mathrm{Re}}\frac{\partial \hat{p}}{\partial \hat{z}} - \frac{2}{\mathrm{Re}}\left(\frac{\partial^2 \hat{w}}{\partial \hat{r}^2} + \frac{1}{\hat{r}}\frac{\partial \hat{w}}{\partial \hat{r}} + \epsilon^2\frac{\partial^2 \hat{w}}{\partial \hat{z}^2}\right) = 0, \tag{18}$$

$$\frac{\partial \hat{u}}{\partial \hat{r}} + \frac{\hat{u}}{\hat{r}} + \frac{\partial \hat{w}}{\partial \hat{z}} = 0, \tag{19}$$

$$\hat{u} = \hat{p}, \quad \hat{w} = 0, \quad \text{on} \quad \hat{r} = 1, \tag{20}$$

$$\hat{p}\Big|_{\hat{r}=1} = \hat{P}_{\mathrm{tm}}, \quad \overline{\hat{w}} = 1, \quad \text{on} \quad \hat{z} = 0, \tag{21}$$

where $\hat{P}_{\mathrm{tm}} = \epsilon R P_{\mathrm{tm}}/(\mu \overline{W}_0)$ is the nondimensional transmembrane pressure at $\hat{z} = 0$. Note that $\hat{P}_{\mathrm{tm}}$ is of order unity. The Reynolds number is defined using the mean axial velocity and inner diameter, $\mathrm{Re} = \rho \overline{W}_0 2R/\mu$. We require,

$$\frac{2}{\mathrm{Re}} \gg \epsilon, \tag{22}$$

so the nonlinear terms in the axial momentum equation (18) are small compared to the pressure and viscous terms. In practice, we treat the ratio $2/Re$ as order unity during the expansion procedure; however, the resulting expansion is typically valid for much larger Reynolds numbers and constraint (22) is actually less restrictive than previous studies. For a filtration system with permeability $\sigma = 10^{-7}$, we expect the solution to hold for Reynolds numbers up to 10^3, and this behavior is confirmed by our numerical simulations. In comparison, the study of Borsi *et al.*[20] restricts Re to order unity or less, regardless of the permeability.

We seek a solution to (17)–(21) in the form of an asymptotic expansion,

$$(\hat{u}, \hat{w}, \hat{p}) = (\hat{u}_0, \hat{w}_0, \hat{p}_0) + \epsilon\,(\hat{u}_1, \hat{w}_1, \hat{p}_1) + O(\epsilon^2). \tag{23}$$

Inserting (23) into (17)–(21) yields a hierarchy of systems of partial differential equations and boundary conditions. Note that for a fixed value of ϵ, it is quite common for asymptotic expansions to become divergent as increasingly higher-order terms are computed.[27] Following common practice, we demonstrate the expansion is consistent to order ϵ and shows excellent agreement with numerical simulation.

We can now clearly differentiate our order-of-magnitude analysis from previous analyses. Galowin and DeSantis[16], Kelsey *et al.*[2], and Borsi *et al.*[20] consider systems of finite axial length L_s, and assume the parameter $\alpha = R/L_\mathrm{s}$ is small, $\alpha \ll 1$. This limits their results to systems of sufficiently long length or small radius. It is not true, however, that increasing the system length, while keeping all other quantities constant, improves the accuracy of their solutions. This is because the system length does not necessarily characterize axial variations of the flow fields. For example, when the permeability tends to zero, $\sigma \to 0$, Poiseuille flow is recovered, and the length scale over which the flow varies axially tends to infinity, $L \to \infty$. This behavior is recovered by the axial length scale, $L = R/\sqrt{\sigma}$, but not L_s. At the other extreme, as the permeability tends to values on the order of unity, $\sigma \sim \mathcal{O}(1)$, the flow field may vary rapidly over an axial length much smaller than the system length. In this case, an expansion about $\alpha = R/L_s$ would not be appropriate, even though α may be small. Our definition of L assures that R/L and ϵ both tend to order unity as $\sigma \to 1$.

Regirer[15] performed an expansion about the small parameter $\beta = u_\mathrm{tm}/\overline{W}_0$, while Denisov[18] performed an asymptotic expansion about the small parameter $\gamma = u_{tm}L_s/(\overline{W}_0 R)$, interpreted as the ratio of the net fluid leaving the membrane to the net axial inflow. By defining their small parameters in terms of the radial and axial flow velocities, the validity of their results are unclear in situations such

as dead-end filtration where β and γ tend to infinity locally.

Our analysis differs from those of Regirer[15], Galowin and DeSantis[16], Denisov[18], Haldenwang[23], and Borsi *et al.*[20] in its treatment of the pressure. Note from the nondimensionalization (16), that ϵ appears in the denominator of $\hat{u}$, but in the numerator of $\hat{p}$. As previously mentioned, this reflects the actual physics of the problem. As the permeability tends to zero, the transmembrane pressure required to drive a small but finite suction tends to infinity. In the filtration literature, this is referred to as the "high-pressure low-recovery" regime. Kelsey *et al.*[2] used a nondimensionalization similar to (16), with the exception that L was replaced by L_s. Our nondimensionalization of u, p, and k makes the application of Darcy's law, $\hat{u} = \hat{p}$ on $\hat{r} = 1$, to the higher-order problems quite simple.

Our definition of L is partially motivated by a previous study by Haldenwang[23] of flows in porous channels. Haldenwang assumed that axial variations of the flow fields scale with the dead-end length, L_{de}. He then found a solution incorporating Darcy's law by expanding in terms of the transverse Reynolds number, $R_{\mathrm{t}} = \rho u_{\mathrm{tm}} H/\mu$, where H was the channel height. Comparing his procedure with ours, we see that R_{t} and L_{de} play roles similar to ϵ and L, respectively.

Order ϵ^0

The zero-order governing equations and boundary conditions are $\partial \hat{p}_0/\partial \hat{r} = 0$, and

$$\frac{\partial^2 \hat{w}_0}{\partial \hat{r}^2} + \frac{1}{\hat{r}} \frac{\partial \hat{w}_0}{\partial \hat{r}} = \frac{\partial \hat{p}_0}{\partial \hat{z}}, \tag{24}$$

$$\frac{\partial \hat{u}_0}{\partial \hat{r}} + \frac{\hat{u}_0}{\hat{r}} + \frac{\partial \hat{w}_0}{\partial \hat{z}} = 0, \tag{25}$$

$$\hat{u}_0 = \hat{p}_0, \quad \hat{w}_0 = 0, \quad \text{on} \quad \hat{r} = 1, \tag{26}$$

$$\hat{p}_0 = \hat{P}_{\mathrm{tm}}, \quad \overline{\hat{w}}_0 = 1, \quad \text{on} \quad \hat{z} = 0. \tag{27}$$

We solve (24)–(26) using separation of variables, $\hat{w}_0 = \hat{w}_0^r(\hat{r})\hat{w}_0^z(\hat{z})$ and $\hat{u}_0 = \hat{u}_0^r(\hat{r})\hat{u}_0^z(\hat{z})$, and find that

$$\hat{w}_0^r = \frac{1}{4}\left(1 - \hat{r}^2\right), \quad \hat{w}_0^z = -\frac{d\hat{p}_0}{d\hat{z}}. \tag{28}$$

$$\hat{u}_0^r = \frac{1}{16}\left(2\hat{r} - \hat{r}^3\right), \quad \hat{u}_0^z = \frac{d^2\hat{p}_0}{d\hat{z}^2}. \tag{29}$$

The zero-order axial flow is similar to a Poiseuille flow with the exception that $d\hat{p}_0/d\hat{z}$ and $\hat{w}_0$ may vary with $\hat{z}$. Substituting (29) into the Darcy condition, $\hat{u}_0 = \hat{p}_0$ on $\hat{r} = 1$, produces an ordinary differential equation for $\hat{p}_0$,

$$\frac{d^2\hat{p}_0}{d\hat{z}^2} - 16\hat{p}_0 = 0. \tag{30}$$

Solving (30) with inlet conditions (27) yields,

$$\hat{p}_0 = -2\sinh(4\hat{z}) + \hat{P}_{\mathrm{tm}}\cosh(4\hat{z}). \tag{31}$$

Order ϵ^1

The first-order governing equations and boundary conditions are $\partial\hat{p}_1/\partial\hat{r} = 0$, and

$$\frac{2}{\mathrm{Re}}\frac{\partial\hat{p}_1}{\partial\hat{z}} - \frac{2}{\mathrm{Re}}\left(\frac{\partial^2\hat{w}_1}{\partial\hat{r}^2} + \frac{1}{\hat{r}}\frac{\partial\hat{w}_1}{\partial\hat{r}}\right) = -\hat{u}_0\frac{\partial\hat{w}_0}{\partial\hat{r}} - \hat{w}_0\frac{\partial\hat{w}_0}{\partial\hat{z}}, \tag{32}$$

$$\frac{\partial\hat{u}_1}{\partial\hat{r}} + \frac{\hat{u}_1}{\hat{r}} + \frac{\partial\hat{w}_1}{\partial\hat{z}} = 0, \tag{33}$$

$$\hat{u}_1 = \hat{p}_1, \quad \hat{w}_1 = 0, \quad \text{on} \quad \hat{r} = 1, \tag{34}$$

$$\hat{p}_1 = 0, \quad \overline{\hat{w}}_1 = 0, \quad \text{on} \quad \hat{z} = 0. \tag{35}$$

Note from (34) that the first-order problem satisfies Darcy's law on the membrane. This is in contrast to Regirer[15] who applied the no-penetration condition $\hat{u}_1 = 0$ on $\hat{r} = 1$. As a result, his higher-order terms do not properly correct the trans-

membrane velocity. We also find the first-order pressure, $\hat{p}_1$, is a function of $\hat{z}$ only. This is in contrast to Granger *et al.*[22] who use an *ad hoc* iterative procedure which assumes that the pressure and viscous terms in the radial momentum equation are of the same order. This leads to an artificial radial dependence in their higher-order pressure corrections, and errors in the axial variation of their higher-order corrections to the velocity fields.

We rewrite the axial momentum equation (32) as,

$$\frac{\partial^2 \hat{w}_1}{\partial \hat{r}^2} + \frac{1}{\hat{r}}\frac{\partial \hat{w}_1}{\partial \hat{r}} = \frac{d\hat{p}_1}{d\hat{z}} + \frac{\mathrm{Re}}{64}\frac{d\hat{p}_0}{d\hat{z}}\frac{d^2\hat{p}_0}{d\hat{z}^2}\left(2 - 2\hat{r}^2 + \hat{r}^4\right), \tag{36}$$

and exploit the linearity of (36) to find a solution to (32)–(34) in the form

$$\hat{w}_1 = \hat{w}_a^r(\hat{r})\hat{w}_a^z(\hat{z}) + \hat{w}_b^r(\hat{r})\hat{w}_b^z(\hat{z}), \tag{37}$$

$$\hat{u}_1 = \hat{u}_a^r(\hat{r})\hat{u}_a^z(\hat{z}) + \hat{u}_b^r(\hat{r})\hat{u}_b^z(\hat{z}), \tag{38}$$

$$\hat{w}_a^r = \hat{w}_0^r, \qquad \hat{w}_a^z = -\frac{d\hat{p}_1}{d\hat{z}}, \tag{39}$$

$$\hat{w}_b^r = -\frac{1}{4608}\left(29 - 36\hat{r}^2 + 9\hat{r}^4 - 2\hat{r}^6\right), \qquad \hat{w}_b^z = \mathrm{Re}\frac{d^2\hat{p}_0}{d\hat{z}^2}\frac{d\hat{p}_0}{d\hat{z}}, \tag{40}$$

$$\hat{u}_a^r = \hat{u}_0^r, \quad \hat{u}_a^z = \frac{d^2\hat{p}_1}{d\hat{z}^2}, \tag{41}$$

$$\hat{u}_b^r = \frac{1}{18432}\left(58\hat{r} - 36\hat{r}^3 + 6\hat{r}^5 - \hat{r}^7\right), \quad \hat{u}_b^z = \mathrm{Re}\left[\left(\frac{d^2\hat{p}_0}{d\hat{z}^2}\right)^2 + \frac{d\hat{p}_0}{d\hat{z}}\frac{d^3\hat{p}_0}{d\hat{z}^3}\right]. \tag{42}$$

The Darcy condition (34) produces an ordinary differential equation for $\hat{p}_1$

$$\frac{d^2\hat{p}_1}{d\hat{z}^2} - 16\hat{p}_1 = -\frac{3\mathrm{Re}}{128}\left[\left(\frac{d^2\hat{p}_0}{d\hat{z}^2}\right)^2 + \frac{d\hat{p}_0}{d\hat{z}}\frac{d^3\hat{p}_0}{d\hat{z}^3}\right]. \tag{43}$$

Solving (43) with the inlet conditions (35) yields

$$\hat{p}_1 = \frac{\mathrm{Re}}{8}\left(4 + \hat{P}_{\mathrm{tm}}^2\right)\left[\cosh(4\hat{z}) - \cosh(8\hat{z})\right] - \frac{\mathrm{Re}\hat{P}_{\mathrm{tm}}}{4}\left[\sinh(4\hat{z}) - 2\sinh(8\hat{z})\right]. \tag{44}$$

Results and discussion

To be consistent with previously published studies of pipe flow, we introduce a new set of nondimensionalized variables,

$$u^* = \frac{u}{\overline{W}_0}, \qquad w^* = \frac{w}{\overline{W}_0}, \qquad p^* = \frac{p}{\rho \overline{W}_0^2}, \qquad r^* = \frac{r}{R}, \qquad z^* = \frac{z}{R}. \tag{45}$$

Using (45), Darcy's law may be written as

$$u^* = \frac{\sigma \mathrm{Re}}{2} p^*, \quad \text{on} \quad r^* = 1. \tag{46}$$

To avoid confusion between P_{tm}, $\hat{P}_{\mathrm{tm}}$, and P^*_{tm}, we define the transmembrane pressure at $z^* = 0$ nondimensionalized with respect to $\rho \overline{W}_0^2$ as,

$$\Pi_{\mathrm{tm}} = \frac{P_{\mathrm{tm}}}{\rho \overline{W}_0^2}. \tag{47}$$

All subsequent equations and variables are nondimensionalized with respect to (45). For notational convenience, we omit the * symbol from the nondimensionalized variables. Using the results in sections and , and recalling that $\epsilon = \sqrt{\sigma}$, the asymptotic expansion may be written as,

$$\begin{aligned} u = \frac{\mathrm{Re}}{32}\left(2r - r^3\right) & \left(\underbrace{\frac{d^2 p_0}{dz^2}}_{\mathcal{O}(\epsilon)} + \underbrace{\sqrt{\sigma}\frac{d^2 p_1}{dz^2}}_{\mathcal{O}(\epsilon^2)} \right) \\ & + \frac{\mathrm{Re}^3}{73728}\left(58r - 36r^3 + 6r^5 - r^7\right) \underbrace{\left[\left(\frac{d^2 p_0}{dz^2} \right)^2 + \frac{dp_0}{dz}\frac{d^3 p_0}{dz^3} \right]}_{\mathcal{O}(\epsilon^2)}, \end{aligned} \tag{48}$$

$$w = -\frac{\mathrm{Re}}{8}\left(1 - r^2\right) \left(\underbrace{\frac{dp_0}{dz}}_{\mathcal{O}(1)} + \underbrace{\sqrt{\sigma}\frac{dp_1}{dz}}_{\mathcal{O}(\epsilon)} \right)$$

$$-\frac{\mathrm{Re}^3}{18432}\left(29-36r^2+9r^4-2r^6\right)\underbrace{\frac{d^2p_0}{dz^2}\frac{dp_0}{dz}}_{\mathcal{O}(\epsilon)}, \tag{49}$$

$$\overline{w}(z)=-\frac{\mathrm{Re}}{16}\left(\frac{dp_0}{dz}+\sqrt{\sigma}\frac{dp_1}{dz}\right)-\frac{3\mathrm{Re}^3}{4096}\frac{d^2p_0}{dz^2}\frac{dp_0}{dz} \tag{50}$$

$$p=\underbrace{p_0}_{\mathcal{O}(1/\epsilon)}+\underbrace{\sqrt{\sigma}p_1}_{\mathcal{O}(1)}, \tag{51}$$

where

$$p_0=-\frac{4}{\sqrt{\sigma}\mathrm{Re}}\sinh(4\sqrt{\sigma}z)+\Pi_{\mathrm{tm}}\cosh(4\sqrt{\sigma}z), \tag{52}$$

$$\begin{aligned}p_1=&-\frac{\mathrm{Re}\Pi_{\mathrm{tm}}}{4}\Big[\sinh(4\sqrt{\sigma}z)-2\sinh(8\sqrt{\sigma}z)\Big]\\&+\frac{1}{16\sqrt{\sigma}}\left(16+\sigma\mathrm{Re}^2\Pi_{\mathrm{tm}}^2\right)\Big[\cosh(4\sqrt{\sigma}z)-\cosh(8\sqrt{\sigma}z)\Big].\end{aligned} \tag{53}$$

For a dead-end filtration system of nondimensional length L_{s} satisfying conditions (6), expressions (48)–(50) for the velocity field remain the same; however, expressions (52)–(53) for the pressure are replaced with:

$$p_0=-\frac{4}{\sqrt{\sigma}\mathrm{Re}}\sinh(4\sqrt{\sigma}z)+\frac{4\coth(4\sqrt{\sigma}\mathrm{L_s})}{\sqrt{\sigma}\mathrm{Re}}\cosh(4\sqrt{\sigma}z), \tag{54}$$

$$\begin{aligned}p_1=&-\frac{\coth(4\sqrt{\sigma}L_{\mathrm{s}})}{\sqrt{\sigma}}\Big[\sinh(4\sqrt{\sigma}z)-2\sinh(8\sqrt{\sigma}z)\Big]\\&+A\cosh(4\sqrt{\sigma}z)-\frac{1}{\sqrt{\sigma}}\Big[\coth^2(4\sqrt{\sigma}L_{\mathrm{s}})+1\Big]\cosh(8\sqrt{\sigma}z),\end{aligned} \tag{55}$$

where

$$\begin{aligned}A=&\frac{\coth(4\sqrt{\sigma}L_{\mathrm{s}})}{\sinh(4\sqrt{\sigma}L_{\mathrm{s}})\sqrt{\sigma}}\Big[\cosh(4\sqrt{\sigma}L_{\mathrm{s}})-\cosh(8\sqrt{\sigma}L_{\mathrm{s}})\Big]\\&+\frac{\sinh(8\sqrt{\sigma}L_{\mathrm{s}})}{2\sinh(4\sqrt{\sigma}L_{\mathrm{s}})\sqrt{\sigma}}\Big[1+\coth^2(4\sqrt{\sigma}L_{\mathrm{s}})\Big].\end{aligned} \tag{56}$$

Returning our attention to solution (48)–(51) for which the transmembrane pressure and mean axial velocity are specified, the orders-of-magnitudes of the various terms in (48)–(51) are indicated using underbrackets. In the limit $\sigma \to 0$, it can be shown using l'Hopital's rule that (48)–(53) recovers classical Poiseuille flow. Consistent with our order-of-magnitude analysis, the leading orders of u, w, and p are $\mathcal{O}(\epsilon)$, $\mathcal{O}(1)$, and $\mathcal{O}(1/\epsilon)$, respectively. The leading-order solution for the axial flow is a Poiseuille flow with a parabolic radial profile, driven by an axial pressure gradient that varies with z. The pressure is a function of z only. A radial pressure dependence does not appear in the asymptotic expansion until p_2, which we do not include here because $p = p_0 + \sqrt{\sigma} p_1$ already shows excellent agreement with direct numerical simulations.

The leading-order terms in (48)–(51) are identical to those of Regirer[15], Granger *et al.*[22], Kelsey *et al.*[2], and Middleman[17]. The higher-order correction terms, however, differ. Regirer's higher-order corrections do not satisfy Darcy's law. The solution of Granger *et al.* contains an artificial radial pressure dependence, as well as errors in the axial variation of the velocity field. Kelsey *et al.*[2] and Middleman[17] do not include the nonlinear convective terms in the Navier-Stokes equation, and their solutions do not have the higher-order corrections that we obtain here. In contrast to Denisov[18], who approximates the axial variation of the flow fields using polynomial functions in z, our analytical solution describes the axial variation through simple cosh and sinh terms. Our solution is more general than that of Kim and Lee[21] for dead-end filtration which requires Bessel functions of the square of the radial coordinate, i.e. $J(r^2)$.

For finite permeabilities, $\sigma \neq 0$, the analytical solution (48)–(51) predicts exponential behavior as $z \to \pm\infty$, due to the cosh and sinh terms. This reflects the physics of the problem, and is confirmed with comparison to direct numerical simulations. Consider, for example, a case where due to axial pressure drop, the pressure in the tube becomes less than that outside the tube, leading to cross flow

reversal at the axial location $z = z_{\mathrm{CFR}}$. As z increases downstream past $z = z_{\mathrm{CFR}}$, injection of fluid into the tube increases the mean axial velocity, decreases the pressure, and further increases the transmembrane injection. As $z \to \infty$, the mean axial velocity and transmembrane injection tend to infinity, as predicted by the analytical solution. This confirms that the approximate solutions of Regirer[15], Kelsey *et al.*[2], and Borsi *et al.*[20], as well as our analytical solution (48)–(51), do not generally improve with increasing system length.

Comparison with direct numerical simulation

We confirm the validity of solution (48)–(51) by comparison with direct numerical simulations (DNS) of the unsteady, two-dimensional, Navier–Stokes and continuity equations in a system of finite axial extent, $-200 \leq z \leq 200$, typical of filtration systems. For this purpose, we modify the Chebyshev pseudo-spectral method of Hugues and Randriamampianina[29] to accommodate Darcy's law on the membrane. Time integration is accomplished using a second-order backward implicit Euler scheme for the linear terms and a second-order explicit Adams-Bashforth scheme for the nonlinear terms. To avoid the numerical singularity on the axis, $r = 0$, the governing equations are multiplied by r^2 and the numerical domain is taken as $(r, z) \in [-1, 1] \times [-200, 200]$. The collocation grid is then chosen to exclude $r = 0$.

The numerical simulation requires boundary conditions on the inlet, $z = -200$, and outlet $z = 200$. One option is to apply the analytical solution (48)–(51) at these locations, but this risks artificially forcing good agreement between the numerical and analytical results. To avoid applying the analytical solution at $z = \pm 200$, we introduce buffer regions near the inlet, $-200 \leq z \leq -160$, and outlet, $160 \leq z \leq 200$, where we multiply the permeability by a function $b(z)$ that tends smoothly to zero at $z = \pm 200$,

$$b(z) = 1 - \left(\frac{z}{200}\right)^{60}. \tag{57}$$

This allows us to apply fully-developed axial flow with a prescribed pressure P_{in} at the inlet,

$$u_{\text{dns}} = 0, \quad \frac{\partial w_{\text{dns}}}{\partial z} = 0, \quad p_{\text{dns}} = P_{\text{in}}, \quad \text{at} \quad z = -200, \tag{58}$$

where u_{dns}, w_{dns}, and p_{dns} are the DNS velocity and pressure fields. At the outlet, we prescribe a Poiseuille flow with a desired mean axial flow $\overline{W}_{\text{out}}$,

$$u_{\text{dns}} = 0, \quad w_{\text{dns}} = 2\overline{W}_{\text{out}}\left(1 - r^2\right), \quad \text{at} \quad z = 200. \tag{59}$$

The numerical simulation is thus completely independent of the analytical solution.

Simulations begin with initial velocity and pressure fields of zero which are integrated in time to steady state. The inlet axial flow rate, transmembrane flow and outlet pressure vary temporally until steady state is reached. Once the flow is steady, we re-scale the DNS flow fields so the mean axial flow rate at $z = 0$ is unity, $\overline{w}_{\text{dns}}(0) = 1$. We then evaluate the DNS transmembrane pressure and Reynolds number at $z = 0$ and use these values for Π_{tm} and Re, respectively, to calculate the corresponding analytical solution (48)–(51) for $-200 \leq z \leq 200$. Because the steady state Reynolds number is unknown *a priori*, it necessarily varies between the different test cases. All test cases have a steady state Reynolds number less than 700 to avoid transition to turbulence which occurs around Re = 2000. We verify spatial resolution from the decay of the spectral coefficients, and use 34 and 257 Chebyshev polynomials in the radial and axial directions, respectively.

To quantify the axial variation of the flow fields, we plot streamlines in the r-z plane, as well as the axial variation of the mean axial velocity, transmembrane velocity and transmembrane pressure. We also measure the percentage axial variation of the DNS transmembrane velocity as,

$$\Delta u_{\text{tm}} = \max_{-150 \leq z \leq 150} 100 \left| \frac{u_{\text{dns}}(1,-150) - u_{\text{dns}}(1,z)}{u_{\text{dns}}(1,-150)} \right|. \tag{60}$$

Test Case	σ	Re	Π_{tm}	$\% \Delta u_{\text{tm}}$	$\% E_0$	$\% E_1$
1 (ultra)	10^{-10}	637.40	19686.15	0.032	3.16×10^{-3}	2.93×10^{-5}
2 (micro)	10^{-9}	540.37	4377.97	0.15	0.029	4.13×10^{-4}
3 (micro)	10^{-7}	473.48	73.62	8.90	2.66	0.035
4 (micro)	10^{-6}	273.39	13.55	64.60	14.16	0.88
5 (AFE)	10^{-6}	153.84	76.77	22.35	13.03	0.64
6 (CFR)	10^{-6}	381.12	1.21	176.99	11.86	0.56

Table 1: The steady state operating conditions for the test cases in the left column: σ, Re, Π_{tm}, Δu_{tm}, E_0, E_1.

From our order-of-magnitude analysis, we expect the error between the analytical and numerical solutions to increase as the axial variation of the flow field, i.e. Δu_{tm}, increases. Naturally, we expect Δu_{tm} to increase with the nondimensional membrane permeability, σ. To quantify the error between the numerical and analytical solutions, we measure the maximum percentage relative error with respect to the transmembrane velocity as,

$$\begin{aligned} E_0 &= \max_{-150\le z\le 150} 100\Big|\frac{u_{dns}(1,z)-u_0(1,z)}{u_{\text{dns}}(1,-150)}\Big|, \\ E_1 &= \max_{-150\le z\le 150} 100\Big|\frac{u_{dns}(1,z)-u(1,z)}{u_{\text{dns}}(1,-150)}\Big|, \end{aligned} \tag{61}$$

where $u_0(1,z)$ is the leading-order analytical solution and $u(r,z)$ is the higher-order analytical solution (48)–(51). To limit artificial errors due to the buffer regions, the quantities Δu_{tm}, E_0 and E_1 are all measured between $-150 \le z \le 150$. Furthermore, because Δu_{tm}, E_0 and E_1 are all normalized with respect to $u_{\text{dns}}(1,-150)$, care is taken to ensure that $u_{\text{dns}}(1,-150)$ is finite in the case of cross flow reversal. As expected, the agreement between the numerical and analytical solutions is best at $z=0$, because the values for Π_{tm} and Re are chosen there, and deteriorates with absolute distance from $z=0$. For all test cases, the maximum errors E_0 and E_1 occur at either $z=150$ or $z=-150$.

Table 1 summarizes the steady state operating conditions for all test cases. The nondimensional permeabilities, σ, and steady state transmembrane pressures, Π_{tm}, of test cases 1 to 4 are typical of ultrafiltration and microfiltration systems. The

nondimensional permeabilities were calculated using experimental values for the ratio of the pure water flux to the applied pressure,[1,28] which is approximately equal to the quantity $\mathcal{K} = k/\mu h$ in Darcy's law, equation (4). From this, $\sigma = \mathcal{K}\mu/R$. Test cases 5 and 6 correspond to axial flow exhaustion and cross flow reversal, respectively, in high permeability microfiltration systems, and serve to test the analytic solution for extreme cases.

Figure 2 illustrates the numerical and analytical results for test case 1, an ultrafiltration system characterized by a high pressure, $\Pi_{\rm tm} = 19686$, low permeability, $\sigma = 10^{-10}$, and nearly constant transmembrane velocity, $\Delta u_{\rm tm} = 0.032$ %. Numerical results are depicted with a dashed line, while the analytical solution (48)–(51) is depicted as a solid line. Panels (b)–(f) illustrate the leading-order solution, u_0, w_0 and p_0, as a dash-dotted line for comparison. Panel (a) shows streamlines, while panels (b), (c) and (d) illustrate the axial variation of the mean axial velocity, transmembrane velocity, and transmembrane pressure, respectively. The buffer regions for the DNS solution have been shaded grey. Panels (e) and (f) illustrate the radial variation of u and w, respectively, at the axial location $z = 150$, where the deviation between the numerical and analytical solutions is expected to be greatest.

In all panels of figure 2, agreement between the higher-order analytical solution and numerical simulation is excellent. The difference between the solid and dashed lines is only visible within the buffer regions of panel (c), where a deviation is expected because the buffer, $b(z)$, modifies the permeability of the numerical simulation so that $u_{\rm dns}$ tends rapidly to zero at $z = \pm 200$. In panel (b), the solid, dashed, and dash-dotted lines are indistinguishable, and the mean axial velocity decreases linearly along the tube. Panels (c) and (d) demonstrate that axial variations of the transmembrane velocity and pressure are small and nonlinear. From Table 1, we note that the numerical and analytical results for the transmembrane velocity agree to within $E_1 = 2.9 \times 10^{-5}$ %. From panels (c) and

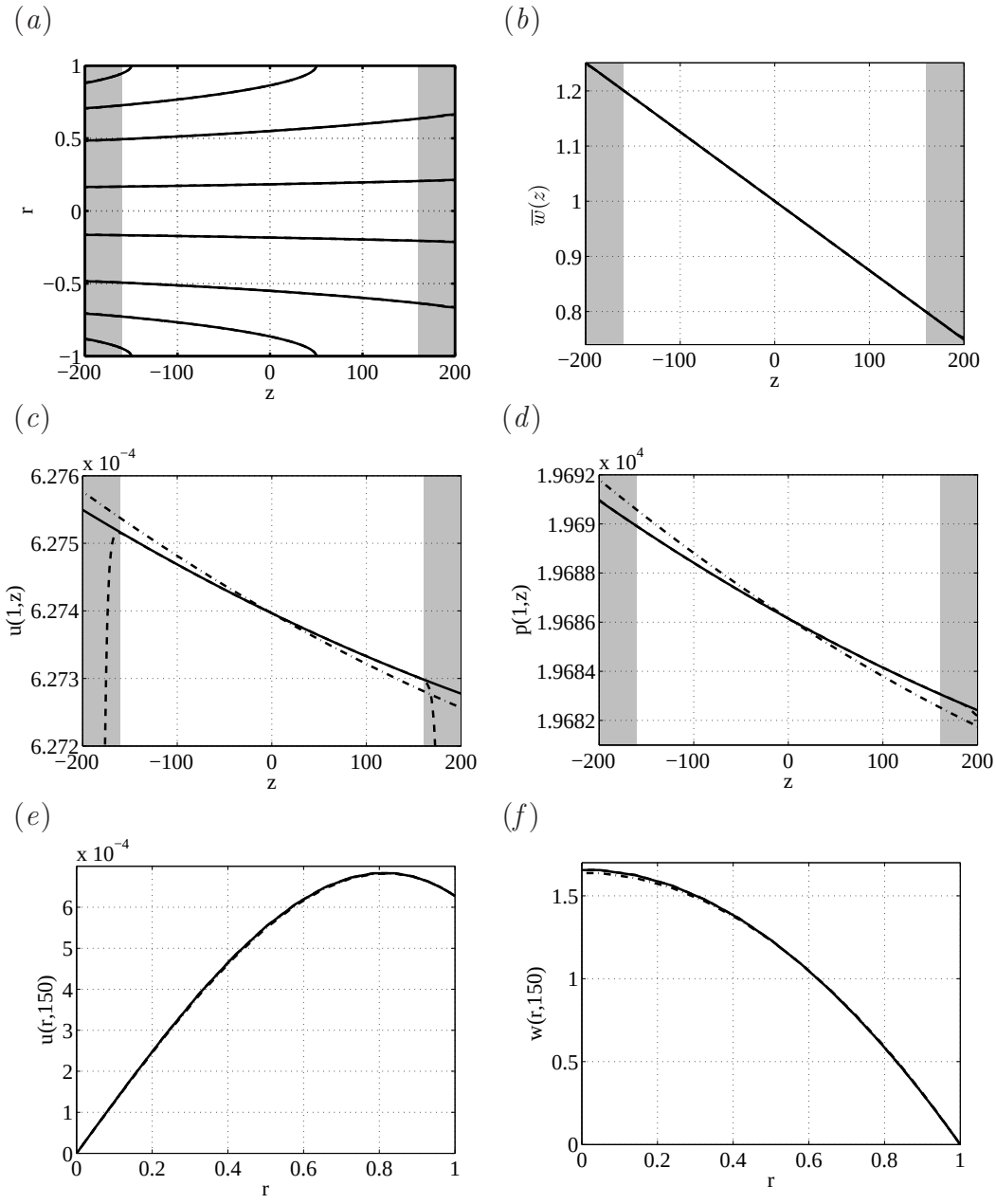

Figure 2: Comparison of the asymptotic expansion (48)–(51) (solid lines) with a direct numerical simulation (dash lines) of ultrafiltration test case 1. The parameters are given in Table 1. In panels (b)–(f), the leading-order solution is depicted with dash-dotted lines. (a) streamlines. (b) mean axial velocity, $\overline{w}(z)$. (c) transmembrane velocity, $u(1,z)$. (d) transmembrane pressure, $p(1,z)$. (e) radial velocity profile, $u(r,150)$. (f) axial velocity profile, $w(r,150)$.

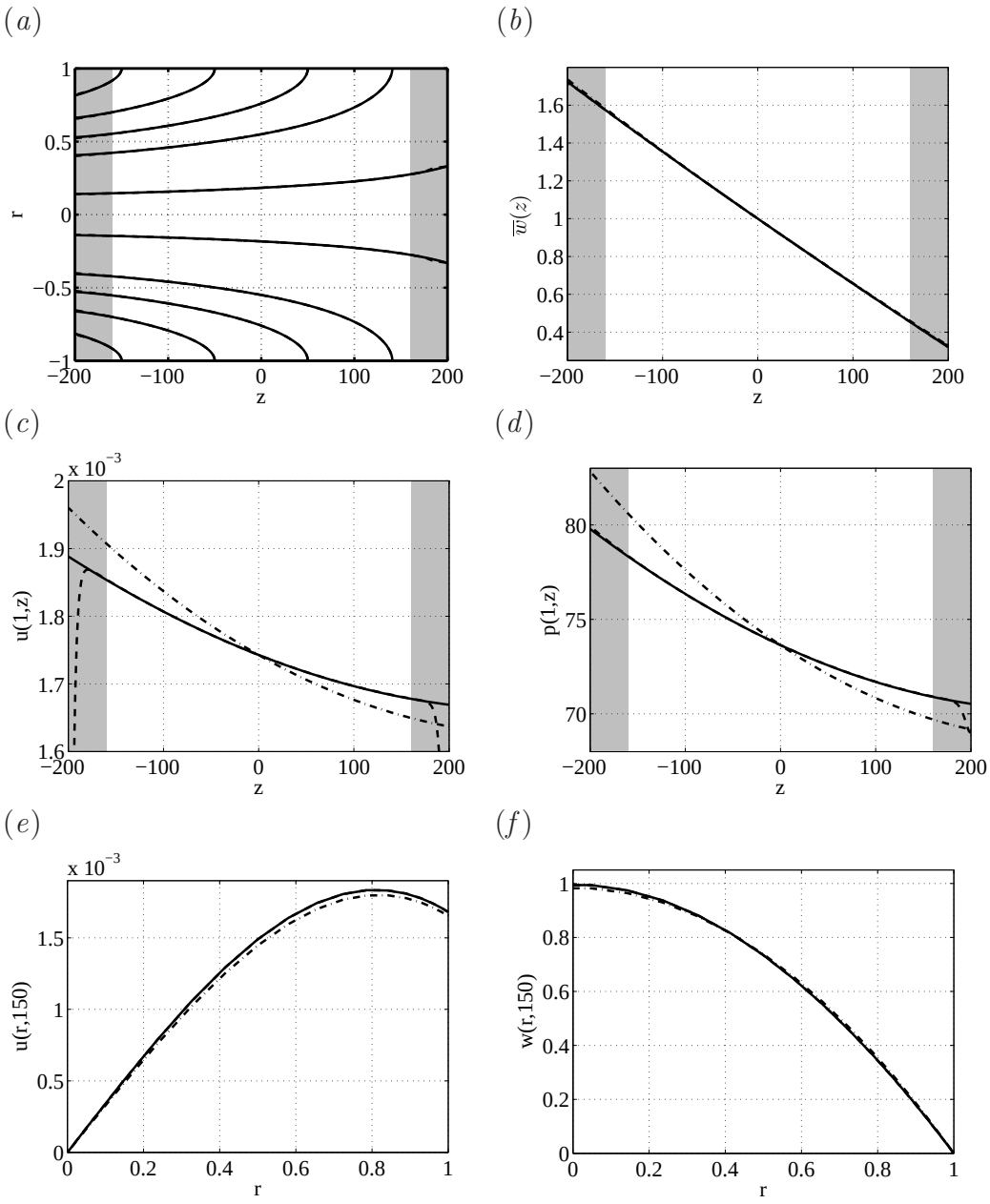

Figure 3: Comparison of the asymptotic expansion (48)–(51) (solid lines) with a direct numerical simulation (dashed lines) of microfiltration test case 3. The parameters are given in Table 1. In panels (b)–(f), the leading-order solution is depicted with dash-dotted lines. (a) streamlines. (b) mean axial velocity, $\overline{w}(z)$. (c) transmembrane velocity, $u(1,z)$. (d) transmembrane pressure, $p(1,z)$. (e) radial velocity profile, $u(r,150)$. (f) axial velocity profile, $w(r,150)$.

(d), it is evident that the leading-order solution does not fully capture the axial variation of the transmembrane velocity and pressure which are over-predicted for $z < 0$ and under-predicted for $z > 0$. The relative error, however, only increases to a very reasonable $E_0 = 3.1 \times 10^{-3}$ %. In figures $2(e)$ and $2(f)$, the numerical and higher-order analytic solutions for the radial variation of u and w are indistinguishable. If the higher-order terms are neglected, a small error is visible between the dashed and dash-dotted lines near the axis in panel (f) where the leading-order solution under-predicts the center-line velocity. Note that due to mass balance in the cylindrical geometry, the radial velocity does not increase monotonically with r. The leading-order solution predicts that u reaches a maximum at $r = \sqrt{2/3}$.

Test cases 2, 3, and 4 correspond to microfiltration systems with increasing permeabilities. In comparison to test case 1, the operating pressure, $\Pi_{\rm tm}$, must be reduced to avoid axial flow exhaustion. As expected, the axial variation of the transmembrane velocity, $\Delta u_{\rm tm}$, and the errors E_0 and E_1 increase with permeability. We found that in the range $10^{-9} \leq \sigma \leq 10^{-8}$, however, the results are very similar to those for case 1: axial variations of the transmembrane velocity are small, and the leading-order solution approximates the DNS results quite well. For this reason, the results for test case 2 are not shown. When the permeability is increased further, $\sigma > 10^{-8}$, axial variations of the flow become more pronounced. Figure 3 illustrates the numerical and analytical results for test case 3, a microfiltration system characterized by $\sigma = 10^{-7}$ and $\Pi_{\rm tm} = 73.6$. The transmembrane suction velocity for test case 3 is an order of magnitude larger than that for case 1, causing the streamlines for test case 3 to curve more towards the membrane. The agreement between the numerical (dashed lines) and full analytic solution (solid lines), however, remains excellent in all panels. The mean axial velocity in figure $3(b)$ varies nearly linearly and is well approximated by the leading-order solution (dash-dotted lines). Note from figure $3(c)$, however, that the axial variation of the transmembrane suction is now significant, $\Delta u_{\rm tm} = 8.90$ %. While it is reason-

able to assume constant transmembrane suction for test cases 1 and 2, assuming constant transmembrane suction for test case 3 could lead to errors on the order of 10 %. The higher-order analytical solution predicts the DNS transmembrane velocity to within $E_1 = 0.039$ %. Panels (c)–(d) illustrate that if the higher-order terms are neglected, the transmembrane suction and pressure are once again over-predicted by the leading-order solution for $z < 0$ and under-predicted for $z > 0$. Note from figures $3(e)$ and $3(f)$ that there is a small discrepancy between the leading-order solution and the DNS results for the radial variation of u and w, the latter indicating that the axial flow profile may no longer be strictly parabolic.

The exponential axial behavior predicted by the analytic solution (48)–(51) becomes more pronounced with increasing permeability. Figure 4 illustrates numerical and analytical results for test case 4, a microfiltration system characterized by a large permeability, $\sigma = 10^{-6}$, small transmembrane pressure, $\Pi_{\rm tm} = 13.55$, and large variation of the transmembrane suction, $\Delta u_{\rm tm} = 64.60$ %. The axial variation of the mean axial velocity in figure $4(b)$ is clearly nonlinear and under-predicted by the leading-order solution (dash-dotted line). Figures $4(c$-$f)$ show that the error between the DNS (dashed lines) and leading-order solution (dash-dotted lines) becomes large, $E_0 = 14.19$ %. The higher-order analytical solution (dashed lines), however, agrees with DNS results quite well, $E_1 = 0.88$ %. In panels (c) and (d), there is a small error between solid and dashed lines in the inlet region, $z \approx -150$. This error has two potential sources. First, the exponential variation of the flow field is greater in the inlet region than the outlet region. As z tends to large upstream values, the axial variations of the transmembrane suction and pressure eventually become large and violate the assumptions of our asymptotic expansion. Second, the downstream influence of the inlet buffer on the DNS solution increases with permeability.

Figure 5 illustrates analytical and numerical results for axial flow exhaustion (AFE) in a microfiltration system characterized by $\sigma = 10^{-6}$, Re = 153.84

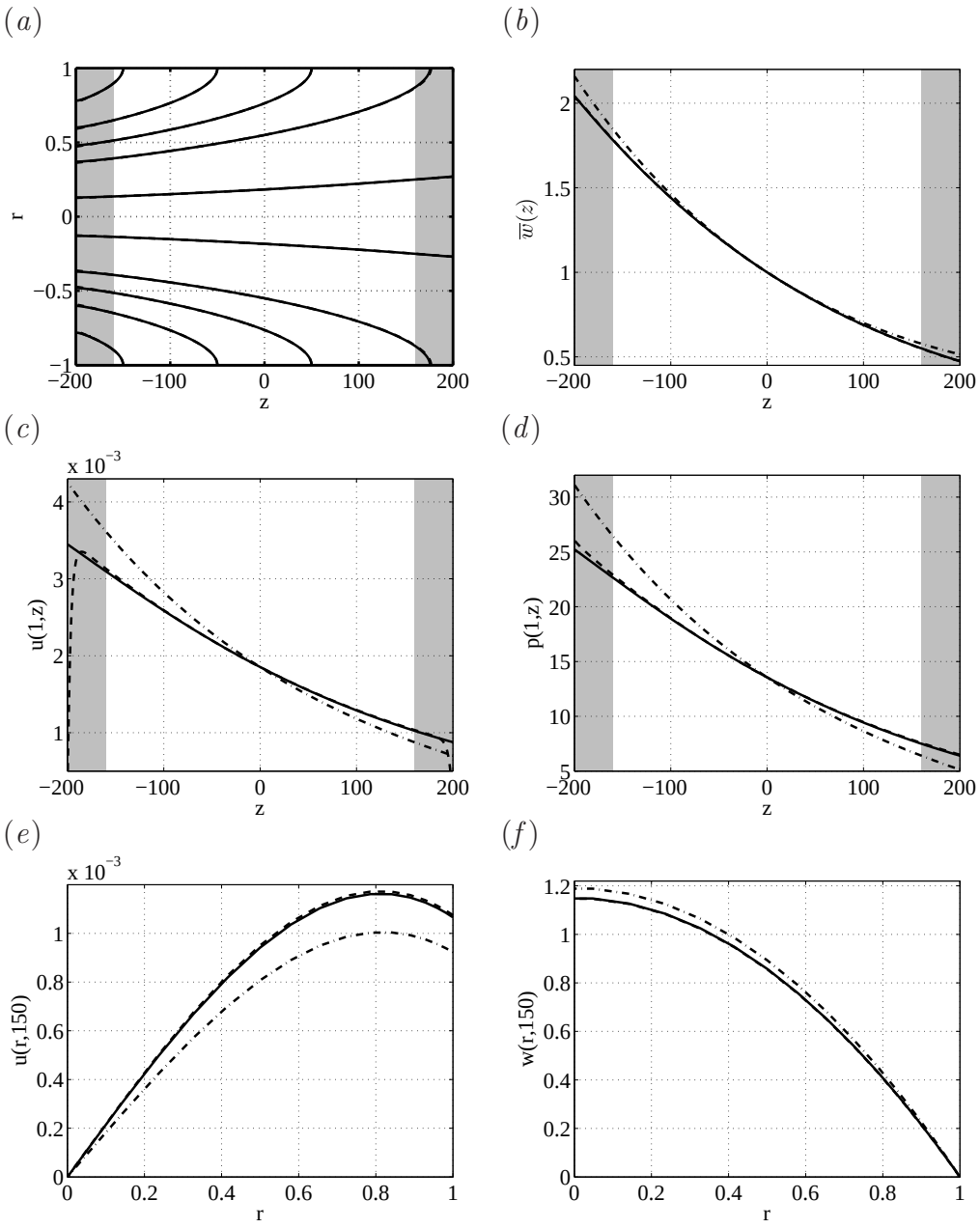

Figure 4: Comparison of the asymptotic expansion (48)–(51) (solid lines) with a direct numerical simulation (dashed lines) of microfiltration test case 4. The parameters are given in Table 1. In panels (b)–(f), the leading-order solution is depicted with dash-dotted lines. (a) streamlines. (b) mean axial velocity, $\overline{w}(z)$. (c) transmembrane velocity, $u(1,z)$. (d) transmembrane pressure, $p(1,z)$. (e) radial velocity profile, $u(r,150)$. (f) axial velocity profile, $w(r,150)$.

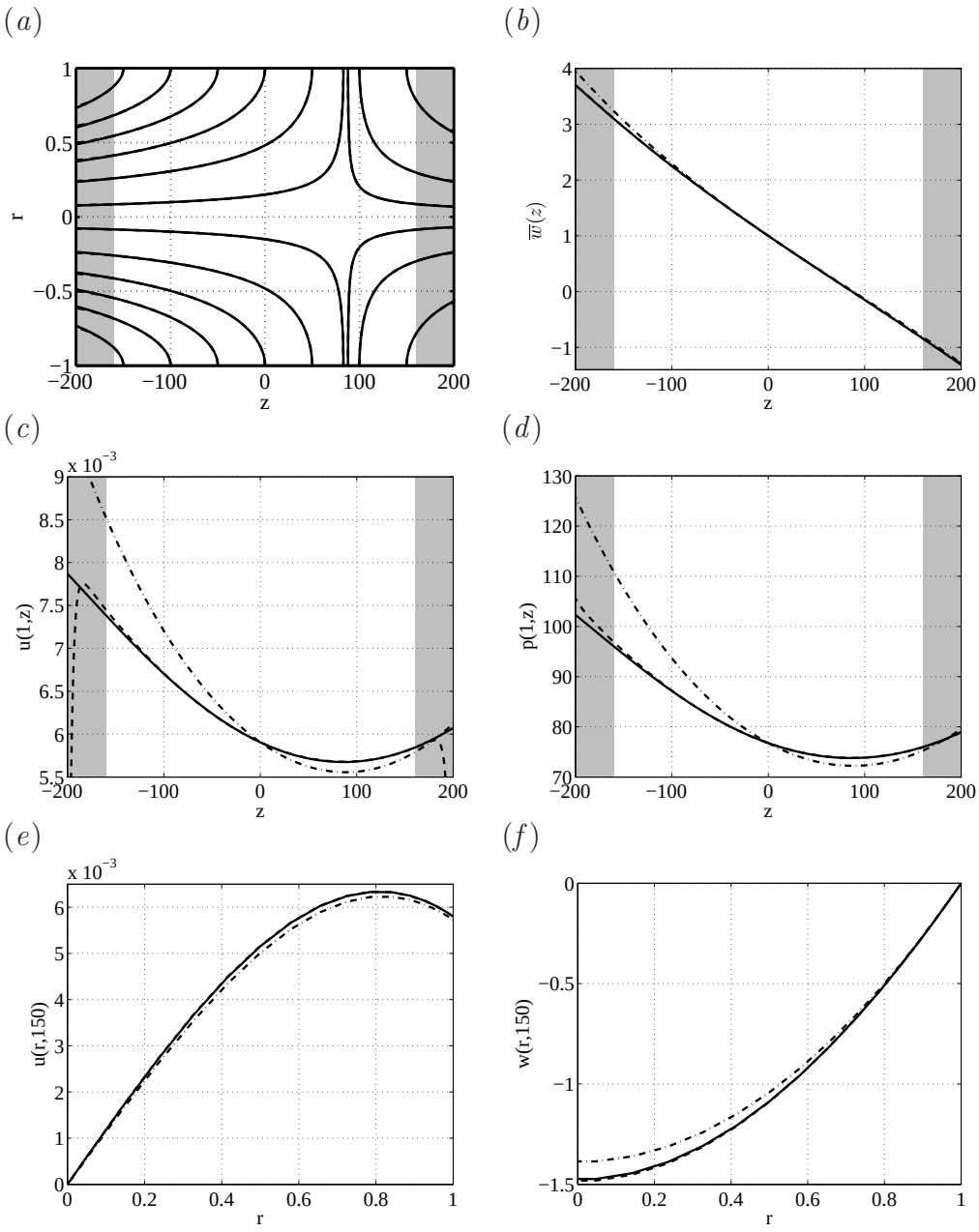

Figure 5: Comparison of the asymptotic expansion (48)–(51) (solid lines) with a direct numerical simulation (dashed lines) axial flow exhaustion in a microfiltration system (test case 5). The parameters are given in Table 1. In panels (b)–(f), the leading-order solution is depicted with dash-dotted lines. (a) streamlines. (b) mean axial velocity, $\overline{w}(z)$. (c) transmembrane velocity, $u(1,z)$. (d) transmembrane pressure, $p(1,z)$. (e) radial velocity profile, $u(r,150)$. (f) axial velocity profile, $w(r,150)$.

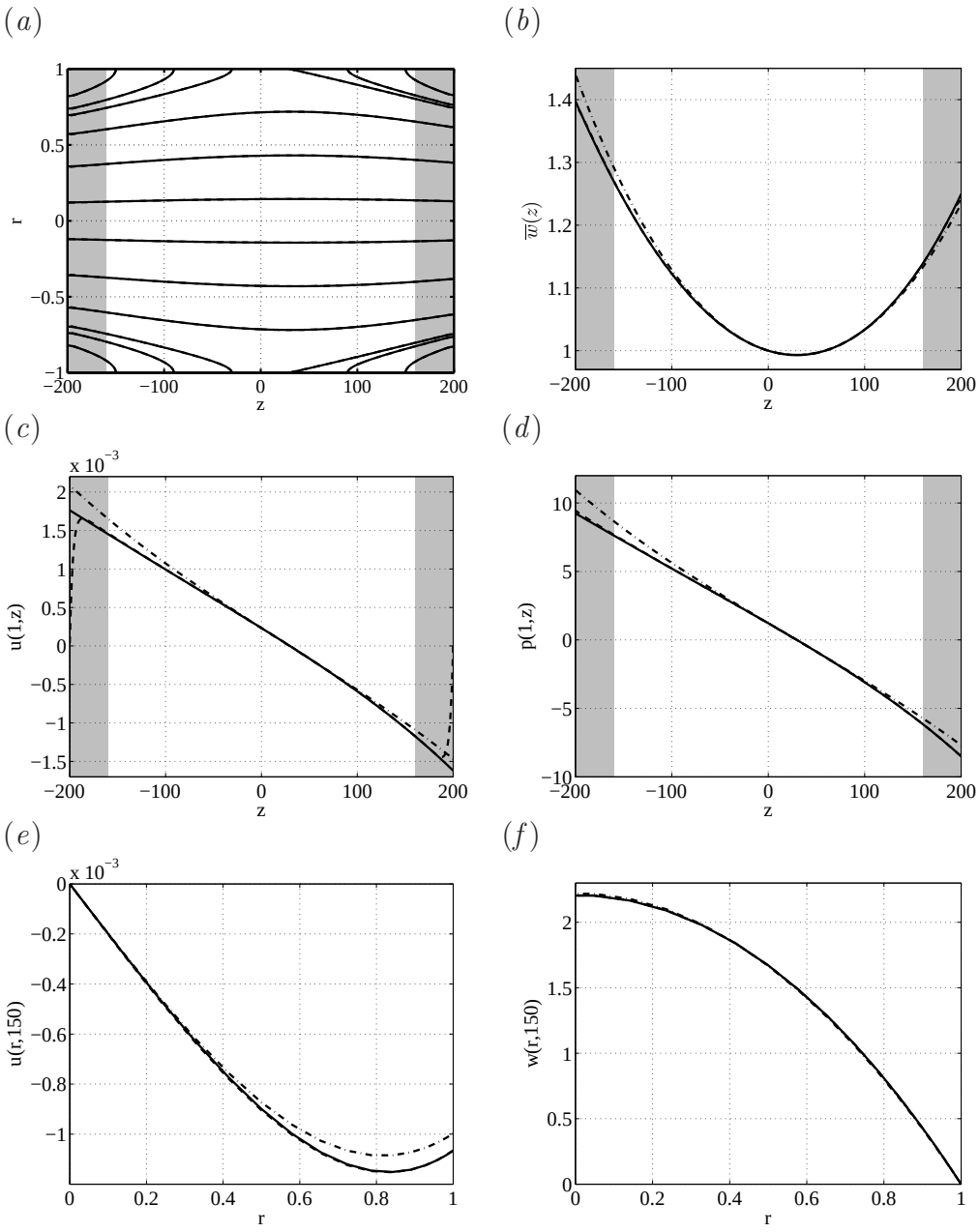

Figure 6: Comparison of the asymptotic expansion (48)–(51) (solid lines) with a direct numerical simulation (dashed lines) of cross flow reversal in a microfiltration system (test case 6). The parameters are given in Table 1. In panels (b)–(f), the leading-order solution is depicted with dash-dotted lines. (a) streamlines. (b) mean axial velocity, $\overline{w}(z)$. (c) transmembrane velocity, $u(1,z)$. (d) transmembrane pressure, $p(1,z)$. (e) radial velocity profile, $u(r,150)$. (f) axial velocity profile, $w(r,150)$.

and $\Pi_{\rm tm} = 76.77$. Exhaustion occurs at $z = z_{\rm AFE}$ where the mean axial flow changes sign, $\overline{W}(z_{\rm AFE}) = 0$, and the transmembrane pressure and velocity are minimized. Consequently, fluid enters the system from both ends. At $z_{\rm AFE}$, the ratio $u(1,z)/\overline{W}(z)$ is infinite, violating relation (8) in the order-of-magnitude analysis. Nevertheless, the agreement between the higher-order analytic solution (solid lines) and DNS solution (dashed lines) is excellent in all panels of figure 5. As observed for case 4, there is a noticeable discrepancy between the solid and dashed lines in the inlet region, $z \approx -150$, of figures 5(c) and 5(d). This is likely due to the fact that AFE occurs downstream of the origin, $z = 0$, and the exponential axial variation of the flow field is more pronounced upstream of $z = 0$. The numerical simulation predicts $z_{\rm AFE} = 86.89$, while the higher-order analytical solution predicts $z_{\rm AFE} = 86.93$, a relative error of only 0.046 %. The leading-order solution predicts $z_{\rm AFE} = 88.15$, a relative error of 1.45 %. Note that the axial velocity profile at $z = 150$, illustrated in figure 5(f), is negative.

Figure 6 illustrates cross flow reversal (CFR) in a microfiltration system characterized by $\sigma = 10^{-6}$, Re = 381.12, and $\Pi_{\rm tm} = 1.21$. Reversal occurs at $z = z_{\rm CFR}$ where the transmembrane pressure and velocity reverse signs, $u(1,z) = p(1,z) = 0$, and the mean axial velocity is minimized. At $z_{\rm CFR}$, relation (12) from the order-of-magnitude analysis is violated. Nevertheless, agreement between the higher-order analytic solution (solid lines) and DNS (dashed lines) remains excellent. The DNS predicts CFR occurs at $z_{\rm CFR} = 29.75$, while the higher-order analytical solution predicts $z_{\rm CFR} = 29.67$, a relative error of 0.27 %. The leading-order solution predicts $z_{\rm CFR} = 29.18$, a relative error of 1.90 %. Due to CFR, the radial velocity profile at $z = 150$, illustrated in figure 6(e), is negative.

Test Case	% E_w	% E_p
1 (ultra)	2.61	4.34×10^{-8}
2 (micro)	4.68	5.52×10^{-7}
3 (micro)	6.92	4.38×10^{-5}
4 (micro)	8.46	4.01×10^{-4}
5 (AFE)	20.04	4.20×10^{-4}
6 (CFR)	3.95	1.13×10^{-3}

Table 2: Results for E_w, see equation (62), and E_p, see equation (63), for all test cases.

Validity of typical assumptions in modelling porous tube flow

Many filtration models assume the transmembrane velocity is constant. From our DNS results for the axial variation of the transmembrane velocity, Δu_{tm}, presented in table 1, it is evident that this is a reasonable assumption for pure filtrate flow under typical operating conditions in reverse-osmosis and ultrafiltration systems, as well as low permeability microfiltration systems for which $\sigma \leq 10^{-8}$. For higher permeabilities, $\sigma > 10^{-8}$, the assumption breaks down and can lead to errors on the order of 10 % for $\sigma \sim 10^{-7}$ and greater than 50 % for $\sigma \sim 10^{-6}$.

Many filtration models[16] assume the axial velocity profile remains parabolic, with a reduction in its mean value, $\overline{w}(z)$, as fluid is removed through the membrane. To explore this assumption, we measure the maximum percentage deviation of the axial DNS velocity field from a corresponding parabolic profile,

$$E_w = \max_{(r,z)\in[0,1]\times[-150,150]} 100\Big|w_{\mathrm{dns}}(r,z) - w_{\mathrm{p}}(r,z)\Big|, \tag{62}$$

where $w_{\mathrm{p}} = 2\overline{w}_{\mathrm{dns}}(z)\,(1-r^2)$ is an axial flow field with a parabolic profile whose mean axial velocity is equal to that of the DNS solution. Because w_{dns} and w_{p} are both nondimensionalized with respect to $\overline{w}_{\mathrm{dns}}(0)$, the error E_w is also automatically normalized with respect to $\overline{w}_{\mathrm{dns}}(0)$. The results, summarized in table 2, show that for typical operating conditions in ultra and microfiltration systems, E_w tends to increase with permeability from $E_w = 2.61$ % for test case 1 ($\sigma = 10^{-10}$) to

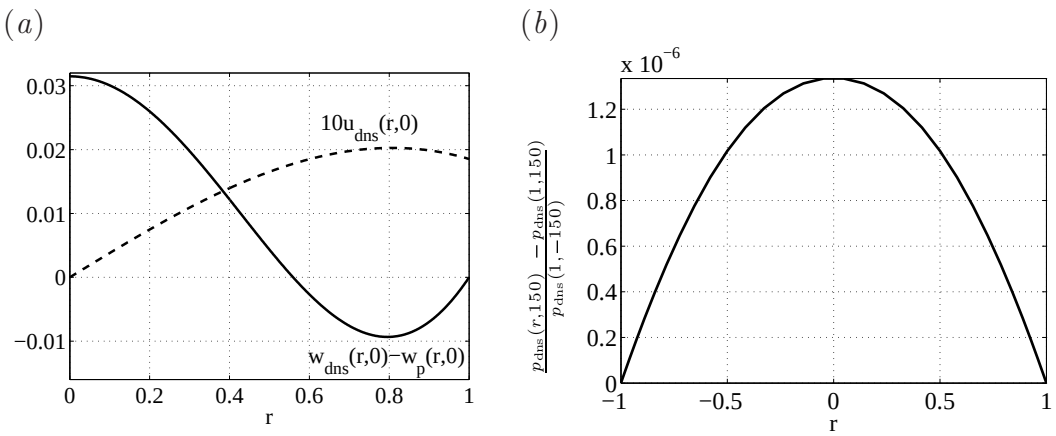

Figure 7: For test case 4 (see table 1), panel (a) shows $w_{\rm dns}(r,0) - w_p(r,0)$ (solid line) and $10u_{\rm dns}(r,0)$ (dashed line), while panel (b) shows the radial variation of $[p_{\rm dns}(r,150) - p_{\rm dns}(1,150)]/p_{\rm dns}(1,-150)$.

$E_w = 8.46$ % for test case 4 ($\sigma = 10^{-6}$).

Figure 7(a) shows the radial variation of $w_{\rm dns} - w_p$ at $z = 0$ for case 4 (solid line), as well as ten times the radial DNS velocity, $10u_{\rm dns}(r,150)$, for comparison. The parabolic profile w_p under-predicts the axial velocity in the center region, $r \lessapprox 0.56$, and slightly over-predicts the axial velocity closer to the wall, $r \gtrapprox 0.56$. The over-prediction is greatest at approximately the same location where $u_{\rm dns}$ is a maximum. This may appear counter-intuitive as one could expect suction to draw high velocity fluid toward the wall, leading to an increase in the velocity near the wall and a decrease in the centerline velocity. We confirmed, however, that the numerical and analytical solutions predict the same behavior.

Lastly, we examine the common assumption that the pressure is constant in radial cross sections, i.e. $\partial p/\partial r = 0$. For this purpose, we measure the maximum percentage radial variation of the DNS pressure field using,

$$E_p = \max_{r\in[0,1]\times[-150,150]} 100\Big|\frac{p_{\rm dns}(r,z) - p_{\rm dns}(1,z)}{p_{\rm dns}(1,-150)}\Big|. \tag{63}$$

The results, presented in table 2, show the radial variation of the pressure is very small for all permeabilities considered, $\sigma \leq 10^{-6}$. Therefore, $\partial p/\partial r = 0$ is a reasonable assumption for pure filtrate flow under typical operating condi-

tions in reverse-osmosis, ultrafiltration, and microfiltration systems. This confirms the validity of our order-of-magnitude analysis, in contrast to the *ad hoc* procedure of Granger *et al.*[22] Figure 7(b) shows the radial variation of $[p_{\rm dns}(r,150) - p_{\rm dns}(1,150)]/p_{\rm dns}(1,-150)$ for test case 4. There is a small negative radial pressure gradient, consistent with the positive radial velocity field.

Conclusions

We successfully devised a robust analytical formulation for incompressible Newtonian flow in a porous tubular membrane that couples the transmembrane pressure and velocity using Darcy's law on the membrane. Using an identical approach, an analogous solution can be found for channel flow between parallel planar porous membranes. This solution is provided in the supplementary material. In comparison to previous studies, we make no assumptions concerning the form of the transmembrane velocity or axial velocity profile. We show that our definitions of the small parameter, $\epsilon = \sqrt{\sigma}$, and axial characteristic scale $L = R/\sqrt{\sigma}$, reflect the physics of the problem more accurately than previous studies. We confirm the validity of our solution with comparison to direct numerical simulations of typical ultrafiltration and microfiltration systems, as well as extreme situations of axial flow exhaustion and cross flow reversal. In all cases, the agreement is excellent.

Using our analytical and numerical results, we demonstrate that the radial pressure gradient, $\partial p/\partial r$, is negligible for all test cases. We also demonstrate that assuming a parabolic radial profile for axial flow may be reasonable for ultrafiltration systems (test case 1), but can lead to errors for high permeability microfiltration systems (test case 4). We further demonstrate that the transmembrane velocity may be reasonably approximated as constant for pure filtrate flow in reverse-osmosis and ultrafiltration systems, as well as low permeability microfiltration systems for which $\sigma \leq 10^{-8}$. We stress, however, that even for these

small permeabilities, the assumption of constant transmembrane velocity cannot realistically model the interaction of solutes or particles with the transmembrane flow via osmotic pressure effects and membrane fouling.

Though not considered here, our approach can be extended to applications where the pressure outside the tube varies slowly in the axial direction, as in the work of Kelsey *et al.*[2]. Though we focus on steady flows, our approach can be extended to flows driven by a pulsatile axial pressure gradient. The next logical step is to extend our asymptotic approach to the study of solute transport, concentration polarization, and the effect of osmotic pressure on the transmembrane flow, as in the work of Denisov[18]. This is left to future work.

The authors would like to acknowledge helpful discussions with Pierre Haldenwang and Mark Johnson and the financial support of the Agence Nationale de la Recherche (program ANR-08-BLAN-0184-03).

Notation

Roman

$b(z)$ permeability buffer, see equation (57)

E_0, E_1 maximum percentage relative error with respect to the transmembrane velocity, see equation (61)

E_p maximum percentage radial variation of p_{dns}, see equation (63)

E_w maximum percentage deviation of w_{dns} from a corresponding parabolic axial flow field w_{p}, see equation (62)

h membrane thickness (m)

k membrane permeability (m^2)

L characteristic length over which axial variations occur, see equations (7) and (15), (m)

L_{de} dead-end length, see equation (9), (m)

p pressure (N/m^2)

$\hat{p}$ pressure, nondimensionalized with respect to (16), $\hat{p} = \epsilon R p/(\mu \overline{W}_0)$

p^* pressure, nondimensionalized with respect to (45), $p^* = p/(\rho \overline{W}_0^2)$

p_{dns} numerical result for pressure, nondimensionalized with respect to (45)

P_{ref} reference pressure outside of tube (N/m^2)

P_{tm} transmembrane pressure at $z = 0$ (N/m^2)

$\hat{P}_{\text{tm}}$ transmembrane pressure at $z = 0$, nondimensionalized with respect to (16), $\hat{P}_{\text{tm}} = \epsilon R P_{\text{tm}}/(\mu \overline{W}_0)$

P characteristic pressure, see equation (7), (N/m^2)

P_{in} inlet pressure of direct numerical simulation, nondimensionalized with respect to (45)

r position in radial direction (m)

$\hat{r}$ radial position nondimensionalized with respect to (16), $\hat{r} = r/R$

r^* radial position nondimensionalized with respect to (45), $r^* = r/R$

R inner radius of tube (m)

Re Reynolds number, $\text{Re} = \rho \overline{W}_0 2R/\mu$

u radial fluid velocity (m/s)

$\hat{u}$ radial velocity, nondimensionalized with respect to (16), $\hat{u} = u/(\epsilon \overline{W}_0)$

u^* radial velocity nondimensionalized with respect to (45), $u^* = u/\overline{W}_0$

u_{dns} numerical result for radial velocity, nondimensionalized with respect to (45)

U characteristic radial velocity, see equation (7), (N/m^2)

Δu_{tm} percentage variation of the DNS transmembrane velocity, see equation (60)

w axial fluid velocity (m/s)

$\hat{w}$ axial fluid velocity, nondimensionalized with respect to (16), $\hat{w} = w/\overline{W}_0$

w^* axial fluid velocity, nondimensionalized with respect to (45), $w^* = w/\overline{W}_0$

w_{dns} numerical result for axial velocity, nondimensionalized with respect to (45)

$\overline{w}$ mean axial velocity (m/s)

$\overline{W}_0$ mean axial velocity at $z = 0$ (m/s)

$\overline{W}_{\text{out}}$ outlet mean axial velocity of direct numerical simulation, nondimensionalized with respect to (45)

z position in axial direction (m)

$\hat{z}$ axial coordinate, nondimensionalized with respect to (16), $\hat{z} = r/L$

z^* axial coordinate, nondimensionalized with respect to (45), $z^* = z/R$

Greek

ϵ nondimensional perturbation parameter, $\epsilon = \sqrt{\sigma}$

κ $\kappa = k/(\mu h)$

μ fluid dynamic viscosity (Ns/m^2)

Π_{tm} transmembrane pressure at $z = 0$, nondimensionalized with respect to (45), $\Pi_{\text{tm}} = P_{\text{tm}}/(\rho \overline{W}_0^2)$

ρ density (kg/m^3)

σ nondimensional permeability, $\sigma = k/(hR)$

References

1. der Bruggen BV, Vandecateele C, Gestel TV, Doyen W, Leysen R. A review of pressure-driven membrane processes in wastewater treatment and drinking water production. *Environmental Progress*. 2003;22:46–56.

2. Kelsey LJ, Pillarella MR, Zydney AL. Theoretical analysis of convective flow profiles in a hollow-fiber membrane bioreactor. *Chem Eng Sci*. 1990;45:3211–3220.

3. Yuan SW, Finkelstein AB. Laminar pipe flow with injection and suction through a porous wall. *Trans ASME*. 1956;78:719–724.

4. White FM. Laminar flow in a uniformly porous tube. *Trans ASME, J Applied Mech*. 1962;29:201–204.

5. Sherwood TR, Brian PLT, Fisher RE, Dresner L. Salt concentration at phase boundaries in desalination by reverse osmosis. *Ind Chem Fund*. 1965;4:113–118.

6. Brady JF. Flow development in a porous channel and tube. *Phys Fluids*. 1984; 27:1061–1067.

7. Bouchard CR, Carreau PJ, Matsuura T, Sourirajan D. Modeling of ultrafiltration: predictions of concentration polarization effects. *J Membr Sci*. 1994; 97:215–229.

8. Wiley DE, Fletcher DF. Computational fluid dynamics modelling of flow and permeation for pressure-driven membrane processes. *Desalination*. 2002; 145:183–186.

9. de Pinho MN, Semiao V, Geraldes V. Integrated modelling of transport processes in fluid/nanofiltration membrane systems. *J Membr, Sci.* 2002;206:189–200.

10. Berman AS. Laminar flows in channels with porous walls. *J App Phys.* 1953; 24:1232–1235.

11. Morel J, Lavan Z, Bernstein B. Flow through rotating porous annuli. *Phys Fluids.* 1977;20:726–733.

12. Marques F, Sanchez J, Weidman PD. Generalized Couette–Poiseuille flow with boundary mass transfer. *J Fluid Mech.* 1998;374:221–249.

13. Kozinski AA, Schmidt FP, Lightfoot EN. Velocity profiles in porous-walled ducts. *Ind Eng Chem Fundam.* 1970;9:502–505.

14. Terrill RM. An exact solution for flow in a porous pipe. *Z Angew Math Phys.* 1982;33:547–552.

15. Regirer SA. On the approximate theory of the flow of a viscous incompressible liquid in a tube with permeable walls. *Sov Phys Tech Phys.* 1960;5:602–605.

16. Galowin LS, Desantis MJ. Theoretical analysis of laminar pipe flow in a porous wall cylinder. *J Dyn Sys, Meas, Control.* 1971;93:102–108.

17. Middleman S. *Modeling Axisymmetric Flows: Dynamics of Films, Jets, and Drops.* Acadeic Press, Inc. 1995.

18. Denisov GA. Theory of concentration polarization in cross-flow ultrafiltration: gel-layer model and osmotic-pressure model. *J Membr Sci.* 1994;91:173–187.

19. Karode SK. Laminar flow in channels with porous walls, revisited. *J Membr Sci.* 2001;191:237–241.

20. Borsi I, Farina A, Fasano A. Incompressible laminar flow through hollow fibers: a general study by means of a two-scale approach. *Z Angew Math Phys*. 2011; 62:681–706.

21. Kim AS, Lee YT. Laminar flow with injection through a long dead-end cylindrical porous tube: Application to a hollow fiber membrane. *AIChE J*. 2011; 57:1997–2006.

22. Granger J, Dodds J, Midoux N. Laminar flow in channels with porous walls. *Chem Eng J*. 1989;42:193–204.

23. Haldenwang P. Laminar flow in a two-dimensional plane channel with local pressure-dependent crossflow. *J Fluid Mech*. 2007;593:463–473.

24. Tilton N, Martinand D, Serre E, Lueptow RM. Pressure-driven radial flow in a Taylor-Couette cell. *J Fluid Mech*. 2010;660:527–537.

25. Beavers GS, Joseph DD. Boundary conditions at a naturally permeable wall. *J Fluid Mech*. 1967;30:197–207.

26. Ochoa-Tapia JA, Whitaker S. Momentum transfer at the boundary between a porous medium and a homogeneous fluid-I. Theoretical development. *Int J Heat Mass Transfer*. 1995;38:2635–2646.

27. Nayfeh AH. *Introduction to Perturbation Techniques*. John Wiley and Sons. 1981.

28. Belfort G, Davis RH, Zydney AL. The behavior of suspensions and macromolecular solutions in crossflow microfiltration. *J Membr Sci*. 1994;96:1–58.

29. Hugues S, Randriamampianina A. An improved projection scheme applied to pseudospectral methods for the incompressible Navier-Stokes Equations. *Int J Numer Meth Fluids*. 1998;28:501–521.